

Deep exclusive π^+ electroproduction off the proton at CLAS

K. Park,^{1,2} R.W. Gothe,² M. Guidal,³ and J.M. Laget¹

(The CLAS Collaboration)

¹Thomas Jefferson National Accelerator Facility, Newport News, Virginia 23606

²University of South Carolina, Columbia, South Carolina 29208

³Institut de Physique Nucleaire ORSAY, Orsay, France

(Dated: February 29, 2012)

The exclusive electroproduction of π^+ above the resonance region was studied using the CEBAF Large Acceptance Spectrometer (CLAS) at the Jefferson Laboratory by scattering a 6 GeV continuous electron beam off a hydrogen target. The large acceptance and good resolution of CLAS, together with the high luminosity, allowed to measure the cross section for the $\gamma^*p \rightarrow n\pi^+$ process in 140 (Q^2 , x_B , t) bins in the phase space domain: $0.16 < x_B < 0.58$, $1.6 \text{ GeV}^2 < Q^2 < 4.5 \text{ GeV}^2$ and $0.1 \text{ GeV}^2 < -t < 5.3 \text{ GeV}^2$. For most bins, the statistical accuracy is of the order of a few percent. Differential cross sections are compared to two theoretical models, based either on hadronic degrees of freedom (Regge phenomenology) or on partonic degrees of freedom (handbag diagram). Both can describe the gross features of the data reasonably well but differ strongly in their approach and in their ingredients. If the handbag approach can be validated in this kinematical region, our data contain the interesting potential to experimentally access transversity Generalized Parton Distributions.

PACS numbers: 13.60.Hb, 25.30.Rw

I. INTRODUCTION

One of the major challenges in contemporary nuclear physics is the study of the transition between hadronic and partonic pictures of the strong interaction. At asymptotically short distances, the strong force is actually weak and the appropriate degrees of freedom are the quarks and gluons (partons) whose interaction can be quantified very precisely by perturbative Quantum Chromodynamics (pQCD). However, at large distances of the order of one Fermi, effective theories taking hadrons as elementary particles whose interactions are described by the exchange of mesons appear more adapted and applicable. The connection between these two domains is not well understood. In order to make progress, the systematic study of a series of hadronic reactions probing these intermediate distance scales is necessary. The exclusive electroproduction of a meson (or of a photon) on the nucleon, $\gamma^*N \rightarrow N'M$, is particularly interesting. Indeed, it offers two ways to vary the scale of the interaction and therefore to study this transition regime. One can vary the virtuality of the incoming photon $Q^2 = -(e - e')^2$, which effectively represents the transverse size of the probe, or the momentum transfer to the nucleon $t = (N - N')^2$, which effectively represents the transverse size of the target. Here, e and e' are the initial and scattered electron four momenta and N and N' are the initial and final nucleon four momenta, respectively. Figure 1 sketches the transition regions that have been experimentally explored up to now (lightly shaded areas) as a function of these two variables, Q^2 and $|t|$. In photoproduction, keeping only $|t| > 3 \text{ GeV}^2$ data, the

relevant experiments are from SLAC [8] and JLab [9]. In electroproduction, keeping only $Q^2 > 1.5 \text{ GeV}^2$ data, the relevant experiments are from Cornell [10, 11], JLab [15] and HERMES [12]. In these latter electroproduction experiments, the phase space was divided into only a few bins in Q^2 , x_B or W , and t . The darkly shaded area in Fig. 1 represent the phase space covered by the present analysis. It is divided into 140 (Q^2 , x_B or W , t) bins.

We also display on Fig. 1 the asymptotically large Q^2 or large $|t|$ partonic diagrams, as well as the low Q^2 and low $|t|$ hadronic diagram, of the $\gamma^*N \rightarrow N'M$ process. At asymptotically large Q^2 and small $|t|$ (vertical axis in Fig. 1), the exclusive electroproduction of a meson should be dominated by the so-called “handbag diagram” [1–4]. The initial virtual photon hits a quark of the nucleon and this same quark, after a single gluon exchange, ends in the final meson. A QCD factorization theorem [4] states that the complex quark and gluon non-perturbative structures of the nucleon are then parametrized in terms of Generalized Parton Distributions (GPDs). For the π^+ channel, at leading twist in QCD, i.e. at asymptotically large Q^2 , the longitudinal part of the cross-section σ_L is predicted to be dominant over the transverse part σ_T . σ_L , in turn, should be dominated by the helicity-dependent GPDs \tilde{E} and \tilde{H} [4] while σ_T is sensitive to the transversity GPDs, dominantly to H_T and $\tilde{E}_T (= 2\tilde{H}_T + E_T)$ [5]. If the asymptotic regime is reached, $d\sigma_L/dt$ should scale as $1/Q^6$ at fixed x_B and $|t|$, while $d\sigma_T/dt$ scales as $1/Q^8$.

At asymptotically large values of $|t|$, i.e. along the horizontal axis in Fig. 1, the $\gamma^*N \rightarrow N'M$ process should be dominated by the coupling of the virtual photon to one of the valence quarks of the nucleon (or of the pro-

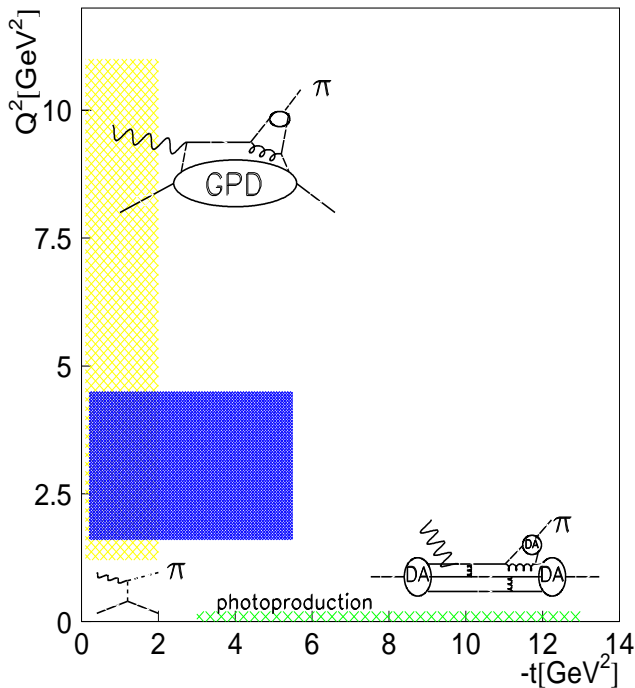


FIG. 1: (Color online) Schematic representation of the $\gamma^* N \rightarrow N' \pi$ process in different regions of the (Q^2, t) plane (above the resonance region): in terms of meson exchanges at low Q^2 and t , in terms of GPDs at large Q^2 and small $|t|$, and in terms of hadron distribution amplitudes (DA) at large $|t|$. The lightly shaded areas (yellow and green online) represent approximately the experimentally explored regions of this phase space up to now. The darkly shaded area (blue online) represents the phase space covered by this analysis.

duced meson), with minimum interaction among the valence quarks. In this regime, a QCD factorization theorem states that the complex structure of the hadrons is parametrized by hadronic distribution amplitudes (DA), which, at small distances (large $|t|$), can be reduced to the simplest configurations of the hadrons (the lowest Fock states), i.e. the 3-quark component of the nucleon and the $q\bar{q}$ component of the meson [6]. At sufficiently high energy, “constituent counting rules” (CCR) can be derived [7] and it is then predicted that such mechanism gives rise to an s^{-7} scaling of the differential cross section $d\sigma/dt$ at fixed center-of-mass pion angles, provided $|s|$, $|t|$, and $|u|$ are all large. Here, s is the squared invariant mass of the γ^* - p system and $u = (\gamma^* - N')^2$ in terms of the four vectors $\gamma^* = e - e'$ and N' . The large $|t|$ and $|u|$ region corresponds typically to a center-of-mass pion angle $\theta_{\text{cm}} \approx 90^\circ$. In particular, the CCR predict $d\sigma/dt = f(\theta_{\text{cm}})s^{2-n}$ for the energy dependence of the cross section, where $f(\theta_{\text{cm}})$ depends on details of the dynamics of the process and n is the total number of point-like particles and gauge fields in the initial and fi-

nal states. For example, our reaction $\gamma^* p \rightarrow n\pi^+$ should have $n = 9$, since there is one initial photon, three quarks in the initial and the final nucleons and two in the final pion.

Open questions remain, including from which Q^2 and from which s do such scaling laws start to appear. Even if these respective scaling regimes are not reached at the presently experimentally accessible Q^2 and s values, can one nevertheless extract useful and universal non-perturbative QCD nucleon-structure information, such as GPDs or DAs, provided some corrections and modifications to the QCD leading-twist mechanisms are applied? Only experimental data can help answer such questions, by looking for the onset of the scaling laws or by comparing the observables to effective calculations, based either on hadronic or partonic degrees of freedom.

II. INSIGHTS FROM PREVIOUS EXPERIMENTS

The two most recent experiments that have measured exclusive π^+ electroproduction off the proton, in the large Q^2 , low $|t|$ regime, where the GPD formalism is potentially applicable, have been conducted in Hall C at Jefferson Lab (JLab) [13–15] and at HERMES [12].

The Hall C experiment, with 2 to 6 GeV electron beam energies, separated the σ_L and σ_T cross sections of the $\gamma^* p \rightarrow n\pi^+$ process by the Rosenbluth technique in the range of $0.17 < x_B < 0.48$ up to $Q^2=3.91$ GeV². It was found that σ_L dominated the cross section for $|t| < 0.2$ GeV² while σ_T was predominant for larger $|t|$ values. These data were compared to two GPD-based calculations, hereafter referred to as VGG [16] and GK [5, 17]. For σ_L , which should be the QCD leading-twist contribution, these calculations were found to be in general agreement with the normalization and the Q^2 - and t -dependencies of the experimental data. In these two calculations, the main contribution to σ_L stems from the \tilde{E} GPD, which is modeled either entirely as pion-exchange in the t -channel [16] or at least dominated by it [5, 17] (see Refs. [18, 19] for the connection between the t -channel pion-exchange and the \tilde{E} GPD). This term is also called the “pion pole”, and the difference between the two calculations lies in the particular choice made for the t -channel pion propagator (Reggeized or not) and the introduction of a hadronic form factor or not at the πNN vertex. In both calculations, σ_L contains higher-twist effects because the pure leading-twist component of the pion pole largely underestimates the data. As to σ_T , only the GK model, which explicitly takes into account higher-twist quark transverse momentum dependence, is able to calculate it. Agreement between data and calculation is found only if the H_T transversity GPD is introduced, which makes up most of the σ_T cross section. In summary, the

normalization and kinematical dependencies of the separated σ_L and σ_T cross sections of JLab Hall C seem to be interpretable in terms of GPD-based models if higher-twist effects, in the form of quark transverse momentum dependence and transversity GPDs, are taken into account.

The HERMES experiment used 27.6 GeV electron and positron beams to measure the $\gamma^*p \rightarrow n\pi^+$ cross section at four (x_B, Q^2) values, with $\langle x_B \rangle$ ranging from ≈ 0.08 to ≈ 0.35 and $\langle Q^2 \rangle$ from ≈ 1.5 GeV² to ≈ 5 GeV². No experimental longitudinal/transverse separation was carried out. The differential cross section $d\sigma/dt$ was compared to the same two GPD models mentioned above. The GK model, which calculates the transverse part of the cross section as well as the longitudinal part, displays the same feature as for the lower energy JLab data, i.e. a dominance of σ_L up to $-t \approx 0.2$ GeV², after which σ_T takes over. The sum of the transverse and longitudinal parts of the cross section calculated by the GK model is in very good agreement with the data over most of the t range measured at HERMES [5, 17]. The VGG model, which calculates only the longitudinal part of the cross section, is in agreement with the data only for low t values [12]. Again, in both calculations, σ_L is dominated by the \tilde{E} GPD, essentially modeled by the pion pole term, and σ_T , in the GK model, is due to transversity GPDs. The HERMES experiment also measured the transverse target spin asymmetry A_{UT} of the $\gamma^*p \rightarrow n\pi^+$ process. The results for that asymmetry have shown [5, 17] that the transversity GPDs H_T or \tilde{E}_T indeed play an important role in the process, confirming the approach of the GK group.

The comparison between the JLab Hall C and HERMES experiments and the two GPD-based calculations yields very encouraging signs that, although higher-twist contributions definitely play a major role and modify the pure leading-twist Q^2 dependencies, there is a possibility to interpret these data in terms of GPDs, in particular transversity GPDs, and therefore to extract some fundamental information on the partonic structure of the nucleon. More precise and more extensive data would be highly useful to confirm these findings. The present experiment covers 20 (x_B, Q^2) bins (with statistical errors of a few percent on average), which doubles or triples the number of bins of the JLab Hall C or HERMES experiments, respectively. These new data are important to test the present GPD-based model calculations and, if the test is successful, bring more stringent constraints on the current GPD parametrizations.

Regarding the large $|t|$ (large $|u|$) domain, where the DA formalism is asymptotically applicable, the $\gamma^{(*)}p \rightarrow n\pi^+$ process has so far been explored only in photoproduction at SLAC [8] at high energies and JLab [20] at lower energies. While the SLAC data tend to follow, for a 90° center-of-mass angle, the s^{-7} scaling asymptotic pre-

diction, the more recent JLab data, which are compatible with the SLAC data but are more precise, actually reveal some large oscillations around this s^{-7} behavior.

In recent years a similar trend, i.e. “global” scaling behavior, has been observed in deuteron photodisintegration experiments [21–24]. It would be interesting to see in exclusive pion electroproduction, i.e. as Q^2 increases, whether one observes a similar scaling behavior and if so, whether the oscillations disappear and the “pure” s^{-7} scaling prediction is reached. The measurement presented in this article is the first one to explore this large $|t|$, large $|u|$, i.e. $\theta_{\text{cm}} \approx 90^\circ$, domain for $\sqrt{s} > 2$ GeV in π^+ exclusive electroproduction off the proton.

III. THE EXPERIMENT

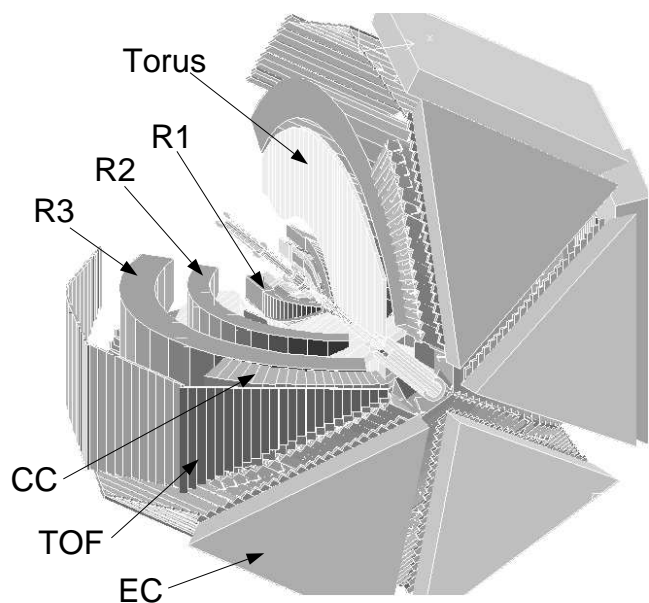


FIG. 2: Three dimensional view of the CLAS detector system.

The measurement was carried out with the CEBAF Large Acceptance Spectrometer (CLAS) [25]. A schematic view of CLAS is shown in Fig. 2. CLAS utilizes a magnetic field distribution generated by six flat superconducting coils (main torus), arranged symmetrically in azimuth. The coils generate an approximate toroidal field distribution around the beam axis. The six identical sectors of the magnet are independently instrumented with 34 layers of drift cells for particle tracking, plastic scintillation counters for time-of-flight (TOF) measurements, gas threshold Cherenkov counters (CC) for electron and pion separation and triggering purposes, and electromagnetic calorimeters (EC) for photon and neutron detection

1 and electron triggering. To aid in electron/pion separation,
 2 the EC is segmented into an inner part facing the
 3 target and an outer part away from the target. CLAS
 4 covers on average 80% of the full 4π solid angle for the
 5 detection of charged particles. The azimuthal acceptance
 6 is maximum at 90° polar angle and decreases at forward
 7 angles. The polar angle coverage ranges from about 8°
 8 to 140° for the detection of π^+ .

9 The scattered electrons are detected in the CC and EC,
 10 which extend from 8° to 45° . The target is surrounded
 11 by a small toroidal magnet (mini-torus). This magnet
 12 is used to shield the drift chambers closest to the target
 13 from the intense low-energy electron background result-
 14 ing from Møller scattering.

15 The specific experimental data set “e1-6” used for this
 16 analysis was collected in 2001. The incident beam had an
 17 averaged intensity of 7 nA and an energy of 5.754 GeV.
 18 The 5-cm-long liquid hydrogen target was located 4 cm
 19 upstream of the CLAS center. The main torus and mini-
 20 torus coils were operated at nominal currents of 3375 and
 21 6000 A, respectively.

22 In this analysis, the two detected particles are the scat-
 23 tered electron and the produced π^+ . The final state is
 24 reconstructed using four-momentum conservation con-
 25 straints. The continuous electron beam provided by CE-
 26 BAF is well suited for measurements involving two or
 27 more final state particles in coincidence, leading to very
 28 small accidental coincidence contributions, smaller than
 29 10^{-3} , for the instantaneous luminosity of $10^{34} \text{ cm}^{-2}\text{s}^{-1}$
 30 of the present measurement.

31 Raw data were subjected to the calibration and recon-
 32 struction procedure that are part of the standard CLAS
 33 data analysis chain. The reaction studied in this pa-
 34 per contributed only a fraction to the total event sam-
 35 ple. Stringent kinematic cuts were applied to select
 36 events with one electron candidate and only one posi-
 37 tively charged track. These events were then subjected
 38 to further selection criteria described in the following sec-
 39 tions. All along the analysis, experimental data distribu-
 40 tions were compared to the output of our Monte Carlo
 41 code GSIM (see next section).

42 A schematic illustration of electron scattering off a nu-
 43 cleon target producing an outgoing nucleon and one pion
 44 is shown in Fig. 3. The scattered electron angle θ_e is given
 45 in the laboratory frame. The two angles, θ_π^* and ϕ_π^* , of
 46 the pion in the center-of-mass frame of the hadronic sys-
 47 tem are defined in Fig. 3. The angle between the virtual
 48 photon three-momentum and the direction of the pion
 49 is denoted as θ_π^* . The angle ϕ_π^* is defined so that the
 50 scattered electron lies in the $\phi_\pi^* = 0^\circ$ half plane with the
 51 z -axis pointing along the virtual photon momentum. For
 52 exclusive single π^+ production off the proton, the final
 53 state neutron is identified by its missing mass, which is
 54 defined by $((e + N) - (e' + \pi))^2$, where π is the four mo-
 55 mentum of the detected π^+ . The kinematic bin size and

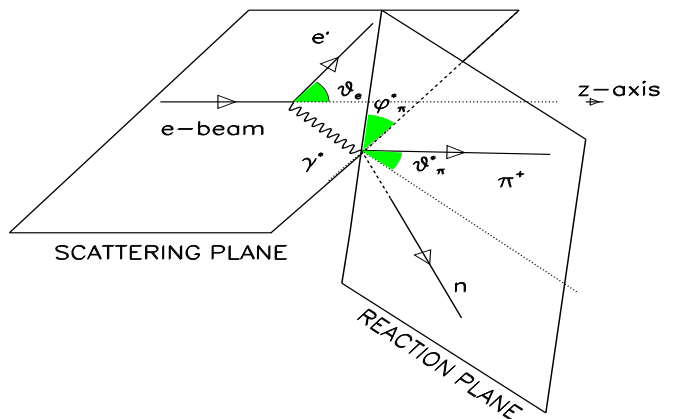


FIG. 3: Kinematics of single exclusive π^+ electroproduction off the proton target.

range are adapted to the accumulated statistics in each bin of interest and summarized in Table I.

TABLE I: The ranges of kinematical bins used in this analysis.

Variable	Number of bins	Range	Bin size
x_B	7	0.16 – 0.58	0.06
Q^2	5	1.6 – 3.1 GeV ²	0.3 GeV ²
	3	3.1 – 4.5 GeV ²	0.5 GeV ²
$-t$	6	0.1 – 1.9 GeV ²	0.3 GeV ²
	3	1.9 – 4.3 GeV ²	0.8 GeV ²
	1	4.3 – 5.3 GeV ²	1.0 GeV ²

IV. THE DATA ANALYSIS

A. Particle identification and event selection

The $\gamma^*p \rightarrow n\pi^+$ reaction channel is identified by detecting the scattered electron in coincidence with a π^+ and by using the missing mass technique to insure the exclusivity of the reaction. A good identification of the electron and pion is therefore the most important issue for the channel identification.

1. Electron identification

The electrons are identified at the trigger level by requiring a minimum amount of energy deposited in EC in coincidence with a signal in CC. For this experiment, the EC hardware threshold was set at a level such that

only electrons with momenta greater than about 640 MeV were detected.

Additional requirements for particle identification (PID) are used in the off-line analysis to refine electron identification. First, we require that the EC and CC hits match geometrically with a reconstructed track in the drift chambers (DC). Second, we correlate the energy deposited in the EC and the momentum obtained by the track reconstruction in the DC. This is aimed at removing the pion contamination.

Indeed, electrons and pions deposit energy in the calorimeter in different ways. Electrons deposit energy in proportion to their incident energy while most of the pions deposit energy in proportion to the thickness of the detector, independently of their energy. The ratio of the total deposited energy in EC to the momentum of particle is called sampling fraction. Approximately 30% of the total energy deposited in the EC is directly measured in the active scintillator material. The remainder of the energy is deposited mostly in the lead sheets interleaved between the scintillator sheets as showering materials. Figure 4 shows the application of the sampling fraction cut to our data. The average sampling fraction for electrons was found to be 0.291 for this experiment. The solid lines in Fig. 4 show the $\pm 3\sigma$ sampling fraction cuts used in this analysis.

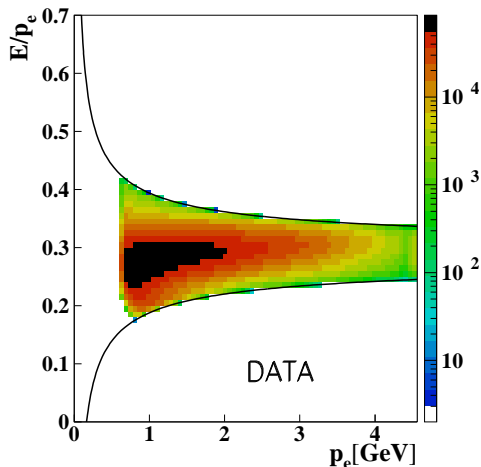


FIG. 4: (Color online) Sampling fraction in EC versus electron momentum for experimental data. The solid curves show the $\pm 3\sigma$ sampling fraction cuts which are applied.

We also requested a minimum energy deposited in the EC to further reject pions. In particular, we asked for the energy deposit in the inner part of EC to be larger than 50 MeV. Most of pions interact as minimum ionizing particles and lose less than this amount in the 15 cm thickness of the inner part of EC.

Another cut was applied to exclude the EC detector

edges. When an electron hit is close to the calorimeter edges, part of the shower leaks outside the device; in this case, the energy cannot be fully reconstructed from the calorimeter information alone. This problem can be avoided by selecting only those electrons lying inside a fiducial volume within the EC that excludes the detector edges. A GEANT based simulation (GSIM) was used to determine the EC-response range with full electron energy reconstruction. The calorimeter fiducial volume was defined by cuts that excluded the inefficient detector regions.

Particle tracks were reconstructed using the drift chamber information, and each event was extrapolated to the target center to obtain an originating vertex location. We demanded that the reconstructed z -vertex position (distance along the beam axis from the center of CLAS, with negative values indicating upstream of the CLAS center) lies in the range $-80 \text{ mm} < z_{\text{vtx}} < -8 \text{ mm}$, as the target center was located at 40 mm upstream from the CLAS center.

Finally, a lower limit on the number of photoelectrons detected in the photomultiplier tubes of the CC for an event provided an additional cut to improve electron identification. The number of photoelectrons detected in CC follows a Poisson distribution modified for irregularities in light collection efficiency for the individual elements of the array. For this experiment, a good electron event was required to have 3 or more photoelectrons detected in the CC.

2. Positively charged pion identification

The main cuts to select the π^+ are based on charge, z -vertex, fiducial cuts and velocity versus momentum correlations. The velocity β is calculated from the ratio of the path length of the track, reconstructed by the drift chambers, to the time of flight, measured by the TOF counters. The momentum is determined from the curvature of the track, reconstructed by the drift chambers, in the main torus magnetic field.

Figure 5 shows the β versus p distribution for positively charged particles from experimental data (top) and from the GSIM Monte Carlo simulation (bottom). A Gaussian is fit to the hadron TOF velocity, depending on their momentum. From the fit, a $\pm 1.5\sigma$ cut on β is chosen for pion candidates as shown in Fig. 5 (solid curves in the plot). Pions and positrons are well separated below 250 MeV of momentum in the experimental data, but this is no longer the case at momenta larger than 400 MeV. For this reason, positrons can be mis-identified as pions, which increases the background. There can also be some particle mis-identification from protons and kaons. We estimated that the missing mass and vertex cuts reduce this mis-identification to the 5%-10% level. This residual

1 background contamination was subtracted as described in
2 in Section VI.

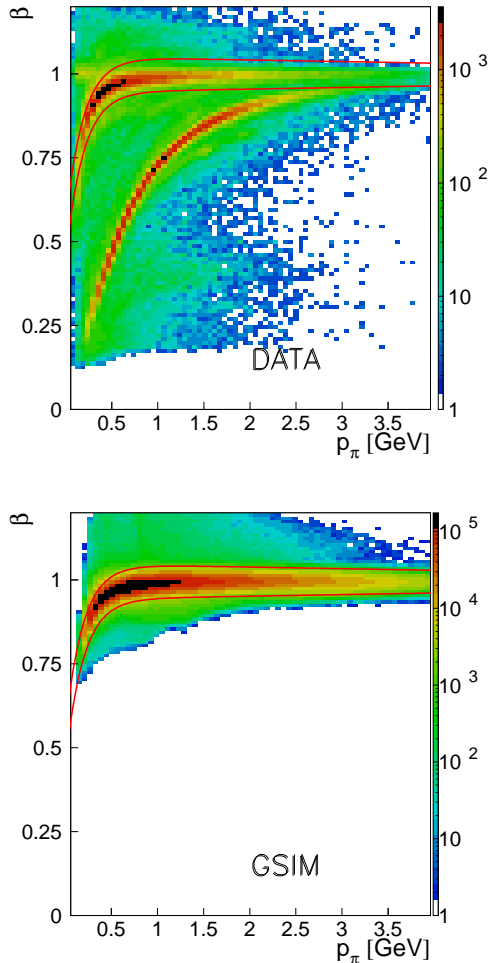


FIG. 5: (Color online) Particle's velocity β versus momentum for π^+ identification, for experimental data (top) and GSIM Monte Carlo simulation (bottom). The solid curves are $\pm 1.5\sigma$ β cut lines for pion candidates.

B. Fiducial cuts

To avoid systematic uncertainties due to the complexity of the geometry and to regions of low or uncertain efficiency of the CLAS detector, we applied fiducial cuts that define the detector regions with nearly full particle acceptance and reconstruction efficiency [26]. The same fiducial cuts are applied in this analysis to both experimental and simulated data.

1. Electron fiducial cuts

The fiducial cuts for electrons were developed to isolate the regions with non-uniform detector efficiency such as the edges of a sector in CC and EC. The fiducial cut is a function of the angles θ_e , ϕ_e , and momentum p_e of the electron. For certain kinematics, less Cherenkov light is collected than under optimal conditions. This effect is observed for specific electron angles (mostly at the lower values of θ_e) and can be seen in Fig. 6 for a certain electron momentum bin in sector 2. In the bottom plots, one sees a central, uniform area, flanked by two fringes, separated by gaps. The solid line in the top plot shows the boundary of the fiducial region for the central momentum in that bin. Only electron events inside the curve (blue area) were used in the analysis.

The criterion used to determine the electron fiducial region in terms of ϕ_e for a given momentum and θ_e bin is the detector efficiency. In order to eliminate the depletion region of the detector, we selected the flat high-efficient areas in the θ_e -sliced ϕ_e distributions. The histograms on the bottom of Fig. 6 show the ϕ_e distributions at two values of $\theta_e = 23^\circ \pm 0.5^\circ$ and $29^\circ \pm 0.5^\circ$. The highlighted area in the center indicates the selected fiducial range. In addition, a set of θ_e versus p_e cuts were used to eliminate the areas with a depleted number of events due to bad time-of-flight counters, photomultiplier tubes in Cherenkov counters, or drift chamber wires.

2. Pion fiducial cuts

The fiducial cuts for pions are defined in a similar way as that used for electrons. The pion fiducial function depends on angles θ_π , ϕ_π , and the momentum p_π . The pion momentum is scanned in 100 MeV steps from 0.3 GeV to 1.7 GeV. The uniform detector efficiency region was determined by selecting a flat high-efficiency ϕ_π region in each θ_π -sliced momentum bin, and the bad TOF counters and the inefficient DC wires were excluded by additional software cuts (the same procedure as was applied to electrons). Figure 7 shows an example for the fiducial cuts for pions in sector 3. The low-efficiency DC regions (between black solid lines and bad TOF paddles between red solid lines on the plot) are removed in both experimental (top) and simulated (bottom) data as part of the fiducial cuts.

C. Kinematic corrections

Empirical corrections to the measured angles and momenta of both electron and pion were applied to account for small imperfection in their trajectory reconstruction. The correction parameters were determined by optimiz-

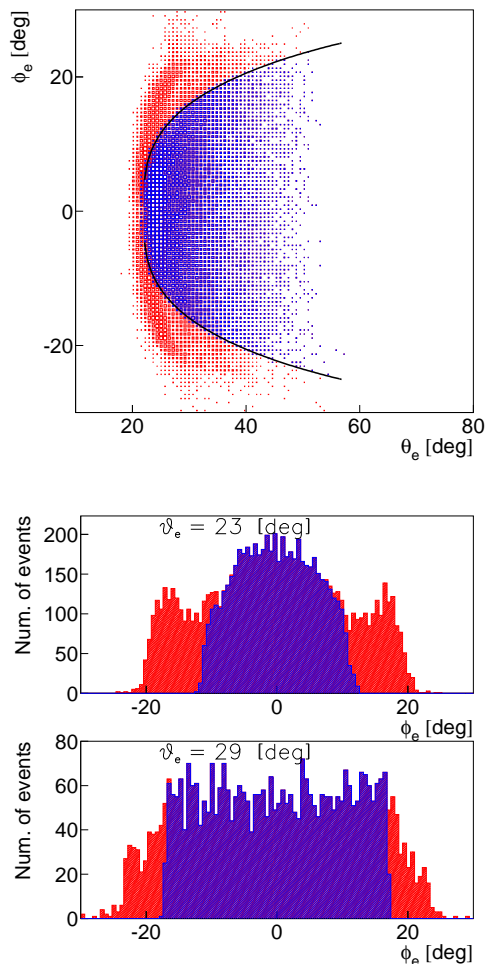


FIG. 6: (Color online) An example of electron fiducial cuts for an electron momentum bin ($p_e = 1.437 \text{ GeV} \pm 25 \text{ MeV}$) in sector 2. See the detailed explanation in the main text.

ing the missing mass peak position to be close to the neutron mass and by minimizing its width. These adjustments were up to 5% of the pion momentum. They resulted in an improved missing mass resolution, from 35 to 23 MeV in average (depending on kinematics). The corrections were most sizable for high-momentum and forward-angle pions present at the high W values of interest in this experiment.

V. MONTE CARLO SIMULATION

In order to calculate the acceptance for the $ep \rightarrow e'\pi^+n$ reaction in the CLAS detector system, we simulated electron and pion tracks using the GEANT-based Monte Carlo Package "GSIM", for the CLAS detector. For sys-

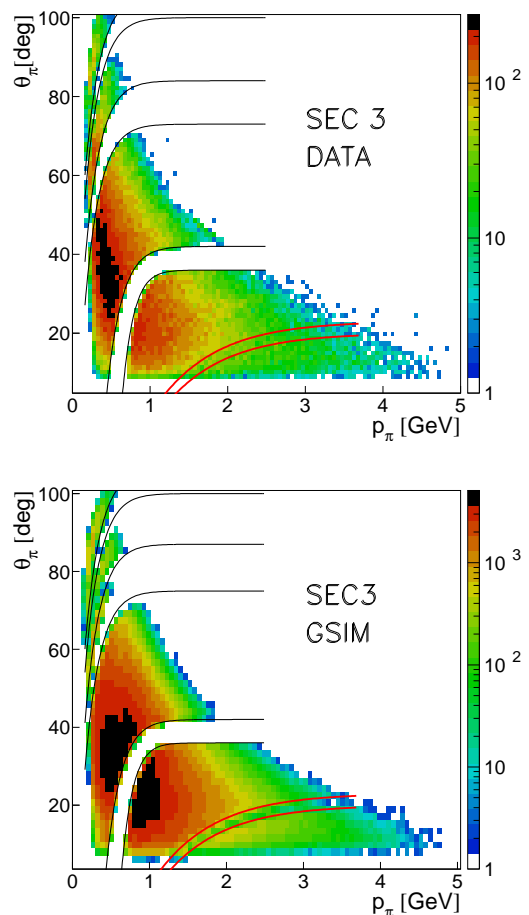


FIG. 7: (Color online) Pion polar angle distribution as a function of momentum in sector 3. The low detector response areas are removed by empirical cuts for experimental (top) and simulated data (bottom). Black thin solid curves are fiducial cuts based on DC and red thick solid curves are bad TOF counters.

tematic checks, we used two Monte Carlo event generators. The first one, called GENEV [27], generates events for various exclusive meson electroproduction reactions, from pion production to the production of vector mesons (ω , ρ^0 , and ϕ), including their decay, radiative effects, resonant and non-resonant multi-pion production, off proton and neutron targets, according to realistic kinematic distributions. For this, it uses cross section tables based on existing photoproduction data and extrapolates to electroproduction by introducing a virtual photon flux factor (Γ) and electromagnetic form factors. Radiative effects, based on the Mo and Tsai formula [28], are part of this event generator as an option. Although the formula is exact only for elastic $e-p$ scattering, it can be used, as a first approximation, to simulate the radiative tail and

to estimate bin migration effects in our pion production process, as will be discussed in section V B. The second event generator that was used is FSGEN [29], which generates events according to the $ep \rightarrow e'\pi^+n$ phase space.

Electrons and positive pions were generated under the “e1-6” experimental conditions. Events were processed through GSIM. We then applied additional ad-hoc smearing factors for the tracking and timing resolutions so that they match the experimental data. The low-efficiency regions in the drift chambers and dead TOF channels were removed during this procedure. Acceptance and radiative corrections were calculated for the same kinematic bins as were used for the yield extraction as shown in Table I. Figure 8 shows the binning applied in this analysis in Q^2 and x_B . The cross sections were then calculated from the yields in each bin, taking into account acceptance and radiative corrections as described below, as well as effective bin sizes.

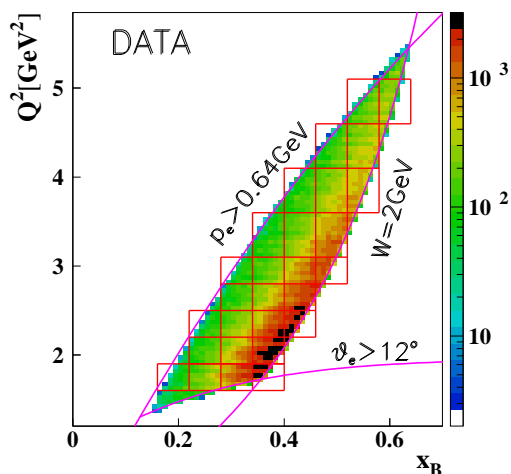


FIG. 8: (Color online) Kinematic coverage and binning (red boxes) as a function of x_B and Q^2 (integrated over all other variables) for experimental data. The events are shown only with $W > 2$ GeV.

We define the acceptance as a function of kinematic variables,

$$Acc(x_B, Q^2, -t, \phi_\pi^*) = \frac{N^{REC}(x_B, Q^2, -t, \phi_\pi^*)}{N^{GEN}(x_B, Q^2, -t, \phi_\pi^*)}, \quad (1)$$

where N^{REC} is the number of reconstructed particles and N^{GEN} is the number of generated particles in each kinematic bin. The overall averaged acceptance is approximately 9%. Figure 9 shows examples of acceptances, determined with the GENEV+GSIM packages, as a function of the pion azimuthal angle ϕ_π^* at a given x_B for various t bins for $Q^2 = 2.35$ GeV².

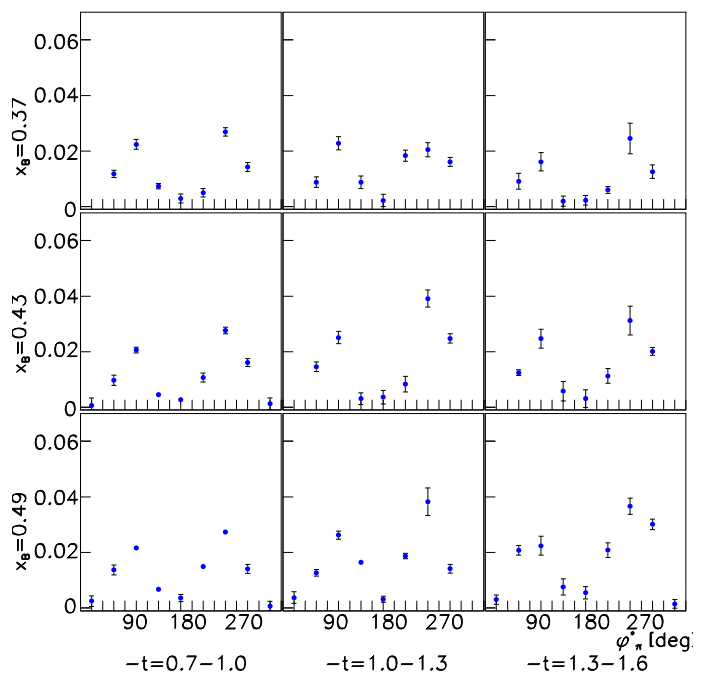


FIG. 9: (Color online) Examples of acceptance as a function of ϕ_π^* for various t and x_B bins at $Q^2 = 2.35$ GeV². The relative dips at $\phi_\pi^* = 0^\circ$ and 180° are due to the sectorized nature of CLAS.

A. Acceptance correction

In order to relate the experimental yields to the cross sections, we calculate the acceptance, including the efficiency of the detector. The acceptance factor (Acc) compensates for various effects, such as the geometric coverage of the detector, hardware and software inefficiencies, and resolution effects from the track reconstruction. We generated approximately 850 million events, taking radiative effects into account, and reconstructed 82 million.

B. Radiative correction

We calculated the radiative correction for our channel in the region $W > 2$ GeV using the complete simulation chain, i.e. using GENEV and GSIM to take into account the effects of the radiation of real photons. These real “Bremsstrahlung” photons can originate either from the primary “hard” scattering at the level of the target proton (“internal” radiation) or, subsequently, from the interaction of the scattered or the initial electron with

the various material layers of the CLAS detector that it crosses (“external” radiation). The GENEV allows to calculate the new value of the incoming electron energy before the reaction takes place. The effects of the radiation of “hard” photons (for instance, the loss of events due to the application of a cut on the neutron missing mass) are already taken care of by the Monte Carlo acceptance calculation described in the previous section. Figure 10 shows examples of the simulated neutron missing mass with and without radiative effects in two W bins, obtained with the GENEV event generator and GSIM. Monte Carlo simulations were carried out with the same cuts and conditions used in the analysis of the experimental data.

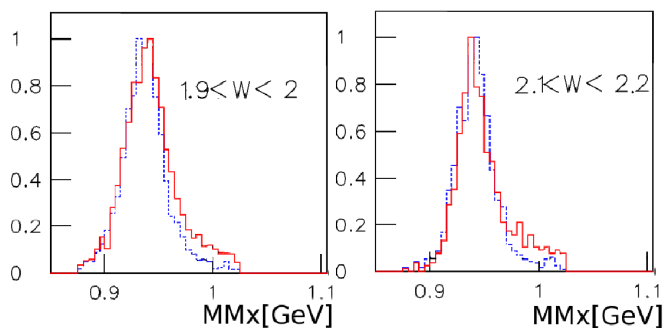


FIG. 10: (Color online) The neutron missing mass distribution from the simulation in two particular W bins with $\Delta W = 100$ MeV for $W = 1.9$ GeV (left) and $W = 2.1$ GeV (right) integrated over ϕ_π^* , $\cos\theta_\pi^*$, and Q^2 . Red solid lines show the normalized yield with radiative effects, and blue dashed lines without.

The correction due to “soft” photons and virtual corrections is determined by extracting the ratio between the number of events without radiative and with radiative effects at the level of the event generator. This radiative-correction factor is calculated for each kinematic bin used in the data analysis.

As a check, the radiative-correction factors were also calculated with the ExcluRad code [30], which contains a complete description of all internal radiative effects in exclusive processes, but currently valid only up to $W = 2$ GeV. We compare the two different radiative-correction methods in a kinematic region where both methods are valid. Figure 11 shows the result of the two methods. It compares the radiative-correction factors in the particular kinematic region $W \approx 1.75$ GeV and $Q^2 \approx 3$ GeV² as a function of $\cos\theta_\pi^*$.

The radiative corrections from ExcluRad are within $\pm 20\%$ over the full $\cos\theta_\pi^*$ range (top). The radiative corrections from GENEV+GSIM also fluctuate around 1.0 with a similar structure (bottom). The error bars

are due to the statistics in our Monte Carlo simulation. Reassured by this relative agreement in this part of the phase space, we use and rely on the GENEV+GSIM radiative-correction factors for our high invariant mass region $W > 2$ GeV. In section VII, we discuss the systematic uncertainty associated to our radiative corrections.

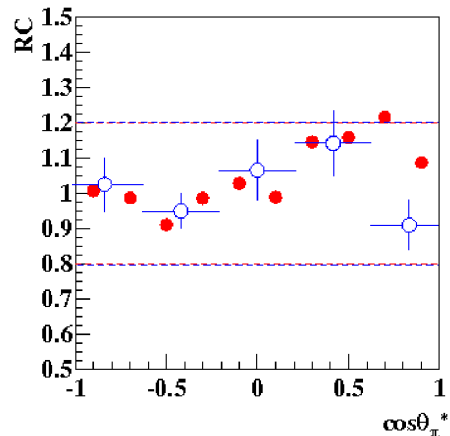


FIG. 11: The radiative-correction factors (RC) as a function of $\cos\theta_\pi^*$ from the calculations by ExcluRad (red solid circle) at $W = 1.74$ GeV, $Q^2 = 3$ GeV², and $\phi_\pi^* = 112.5^\circ$ and by the GSIM simulation (blue open circle) at $W \approx 1.75$ GeV, $Q^2 \approx 3$ GeV² and $80^\circ < \phi_\pi^* < 120^\circ$.

VI. BACKGROUND SUBTRACTION

There are two main sources of background in our reaction. One consists of the mis-identification of pions with other positively charged particles (protons, kaons, positrons). This is particularly important for the pion-proton separation at high momenta ($p > 2$ GeV), see section IV A. The other one consists of multi-pion production. To subtract both backgrounds, we fit the neutron missing mass distribution bin-by-bin. The background was fit by an exponential plus a Gaussian. This latter function was determined from simulations of the multi-pion spectra in the neutron missing mass region > 1.02 GeV.

Figure 12 (top) shows an example of such a background fit. A comparison of the missing mass spectrum is shown in the bottom plot of Fig. 12 before (black squares) and after (red circles) background subtraction. In the range of the neutron missing mass cut, shown by the two vertical lines (0.877 GeV \leq MMx \leq 1.0245 GeV), the background is small, and the remaining radiative tail becomes visible after the background is subtracted.

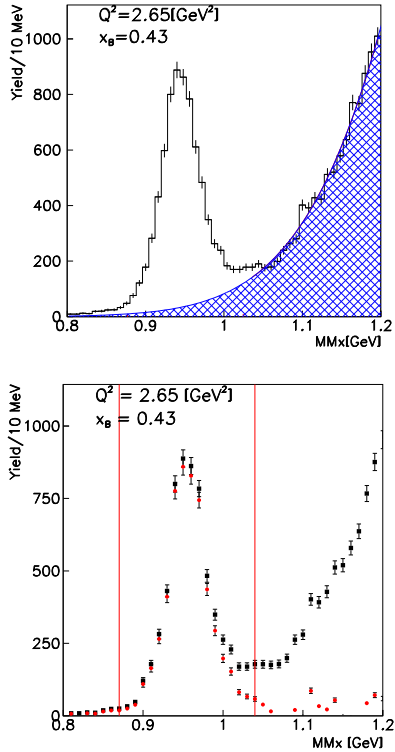


FIG. 12: (Color online) An example of background distribution under the neutron missing mass at $Q^2 = 2.65 \text{ GeV}^2$, $-t = 1.15 \text{ GeV}^2$, and $x_B = 0.43$ (top), and another before (black boxes) and after (red circles) background subtraction (bottom). The two vertical lines represent the neutron missing mass cut used in this analysis.

VII. SYSTEMATIC UNCERTAINTIES

Several sources of systematic uncertainties that can affect our measurements have been studied by changing various cuts and using different event generators.

We varied the criteria used for the particle identification to provide more stringent or less stringent particle selection and redoing the complete analysis. The cuts on EC energy deposition and extrapolation of the CC amplitude for the electron as well as cuts on the TOF timing for the pion have been varied. The EC sampling fraction cut (cut at $\pm 3\sigma_{EC}$ versus cut at $\pm 2\sigma_{EC}$ from the average value) led to a 5% uncertainty for electron identification. The TOF β cut ($\pm 2\sigma_{TOF}$ cut versus $\pm 2.5\sigma_{TOF}$ cut on the peak value) for pion identification gives a 1.7% uncertainty. The various cuts for channel identification such as fiducial, missing mass, and vertex cuts produced 3%, 1%, and 1.6% of systematic uncertainties, respectively.

Acceptance and radiative corrections are the biggest sources of systematic uncertainties in this analysis. The

systematic uncertainty for the acceptance calculation is evaluated by comparing our results using the GENEV and FSGEN event generators. In the limit of infinitely large statistics and infinitely small size bins, our acceptances should be model-independent (up to the bin-migration effects). This is not exactly the case here and we find differences of about $\approx 5\% \pm 3\%$. The systematic uncertainty for the radiative correction is estimated similarly by comparing the radiative-correction factors (GENEV and ExcluRad). We calculated the difference between the cross-sections corrected for radiative effects using on the one hand, GENEV and on the other hand, the W -expanded ExcluRad (where ExcluRad was linearly extrapolated to $W > 2 \text{ GeV}$). An average 8% systematic uncertainty is found. Acceptance and radiative corrections are actually correlated, but after a combined analysis we estimated an average 9.5% total uncertainty for both effects.

Concerning the background subtraction procedure under the neutron missing mass (section VI), we used various fitting functions (Gaussian plus exponential, Gaussian plus polynomial, exponential plus polynomial, etc...). These various fitting functions eventually produced very small differences and we estimated a $< 1\%$ systematic uncertainty associated to this procedure.

These latter systematic errors were determined for each individual bin. Concerning overall scale errors, the target length and density have 1% of systematic uncertainty and the integrated charge uncertainty is estimated to 2%. The total systematic uncertainty, averaged over all bins, is approximately $\approx 12\%$.

VIII. RESULTS AND DISCUSSION

In this section, we present our results for the cross sections of the $p(e, e'\pi^+)n$ reaction in the invariant mass region $W > 2 \text{ GeV}$. We have extracted the differential cross sections as a function of several variables (t , Q^2 , and W or x_B), with the other variables being fixed, except ϕ_π^* , which is always integrated over. The error bars on all cross sections include both statistical and systematic uncertainties added in quadrature.

A. $d\sigma/dt$ as a function of t

We begin by presenting in Fig. 13 the differential cross section $d\sigma/dt$ as a function of t for different (x_B , Q^2) bins. The differential cross section $d\sigma/dt$ is the “reduced” cross section where the virtual photon flux factor has been factorized out,

$$\frac{d\sigma}{dt} = \frac{1}{\Gamma} \frac{d^3\sigma}{dQ^2 dx_B dt},$$

and where ϕ_π^* is integrated over.

We have included in Fig. 13 the JLab Hall C data (light-blue squares [13, 14] and open star symbol [15]), which cover only the very small t domain. The JLab Hall C data central (t , Q^2 , and W or x_B) values do not exactly match our central (t , Q^2 , and W or x_B) kinematics but are sufficiently close to allow for a reasonable comparison.

We note that there is in general a good agreement between the results of the two experiments. For a better visualization, which is also relevant for the comparison with the models in the following, we also show Fig. 14 which concentrates on the low $|t|$ range of Fig. 13.

As could be expected, the $d\sigma/dt$ cross sections fall in general in an exponential way as $|t|$ increases, with some flattening at large $|t|$, which are features that are also observed in photoproduction [8, 20]. For several bins, for instance $(x_B, Q^2)=(0.31, 1.75)$ or $(0.37, 2.05)$, we notice a structure in $d\sigma/dt$ for $-t \approx 0.5 \text{ GeV}^2$. The origin of this “dip” is not known to us but it is a priori physical since its amplitude is clearly stronger than the size of our error bars. We remark that the JLab Hall C experiment [14] also measured such a structure in $d\sigma/dt$ (see their Fig.13 [14] and for instance the bin $(W, Q^2)=(1.8, 2.16)$).

We first compare our data to a calculation based on hadronic degrees of freedom. This calculation is the Laget model [31] based on Reggeized π^+ and ρ^+ meson exchanges in the t -channel [32]. The hadronic coupling constants entering the calculation are all well known or well constrained and the main free parameters in this approach are the mass scales of the electromagnetic form factors at the photon-meson vertices.

If one considers only “standard” monopole Q^2 -dependent form factors, one obtains much steeper t -slopes than the data. An agreement with the data can be recovered by introducing a form factor mass scale that also depends on t , according to the prescription of Ref. [31]. This form factor accounts, in a phenomenological way, for the shrinking in size of the nucleon system as t increases (as was mentioned in our introduction). The results of this calculation, i.e. with (Q^2, t) -dependent meson electromagnetic form factors, are shown, for $d\sigma_T/dt$, $d\sigma_L/dt$, and $d\sigma/dt = d\sigma_T/dt + \epsilon d\sigma_L/dt$, in Figs. 13 and 14 by the red curves. The Laget model gives a qualitative description of the data, i.e. of their overall normalization at low t and x_B -, Q^2 - and t - dependencies. We recall that this model already gives a good description of the photoproduction data (SLAC, JLab) and of the HERMES electroproduction data, and that the form factor mass scale [31] has not been adjusted to fit our data.

In the framework of this model, $d\sigma_L/dt$ is dominating at low $|t|$ values while $d\sigma_T/dt$ takes over around $-t \approx 0.5 \text{ GeV}^2$, this value being approximately the same for all (Q^2, x_B) bins. This dominance of σ_L at low $|t|$ is, as was mentioned in the introduction, a consequence of the

t -channel π^+ -exchange (pion pole). At larger $|t|$, the ρ^+ meson exchange, which contributes mostly to the transverse part of the cross section, begins to dominate. The Laget Regge model, in addition to t -channel meson exchanges, also contains u -channel baryon exchanges. It thus exhibits at the largest $|t|$ values, corresponding to low $|u|$ values, an increase of the cross section in some (Q^2, x_B) bins. We have additional data at larger $|t|$ values (i.e. lower $|u|$ values) which are currently under analysis. They will be published in the near future and the physics discussion will focus on these “backward” mechanisms.

We now turn to the partonic approach of the GK model that is based on the handbag GPD formalism. We recall that in this model $d\sigma_L/dt$ is, like for the Laget Regge model, mostly generated by the pion pole. There are, however, a couple of important differences in the treatment of this pion pole in the two calculations. In the Laget model, it has, firstly, an intrinsic energy dependence. Indeed, it is “Reggeized”, i.e. the t -channel propagator is proportional to $s^{\alpha_\pi(t)}$, where $\alpha_\pi(t)$ is the pion Regge trajectory. Secondly, as mentioned in the previous paragraph, it is associated with a (Q^2, t) -dependent electromagnetic form factor. These two features change the s - (or x_B -) and t - dependencies of the pion pole with respect to the GK treatment. Indeed, in this latter case, the t -channel pion propagator is proportional to $1/(t - m_\pi^2)$, i.e. it has no energy dependence, and the hadronic form factor at the πNN vertex is only t -dependent.

Figures 13 and 14 also show the results of the GK calculation (in blue) for $d\sigma_L/dt$ and $d\sigma/dt$. We see that $d\sigma_L/dt$ has a non-negligible contribution only in the low $|t|$ domain and only for a few (x_B, Q^2) bins, in particular at the lowest x_B and the largest Q^2 values. This is in line with the observation that we mentioned in section II that, at HERMES kinematics, i.e. at lower x_B and larger Q^2 values, the GK model displayed a strong dominance of the longitudinal part of the cross section, at low $|t|$. When one explores a larger (Q^2, x_B) phase space, as in the present experiment, one sees that, at least theoretically, the dominance of $d\sigma_L/dt$ at low $|t|$ is not at all systematic in the GK calculation. The ratio of $d\sigma_L/dt$ to $d\sigma/dt$ strongly depends on x_B . Specifically, it decreases as x_B increases and at $x_B=0.49$, $d\sigma_L/dt$ is only a few percent of $d\sigma/dt$, even at the lowest t values. This is a notable difference from the Laget Regge model.

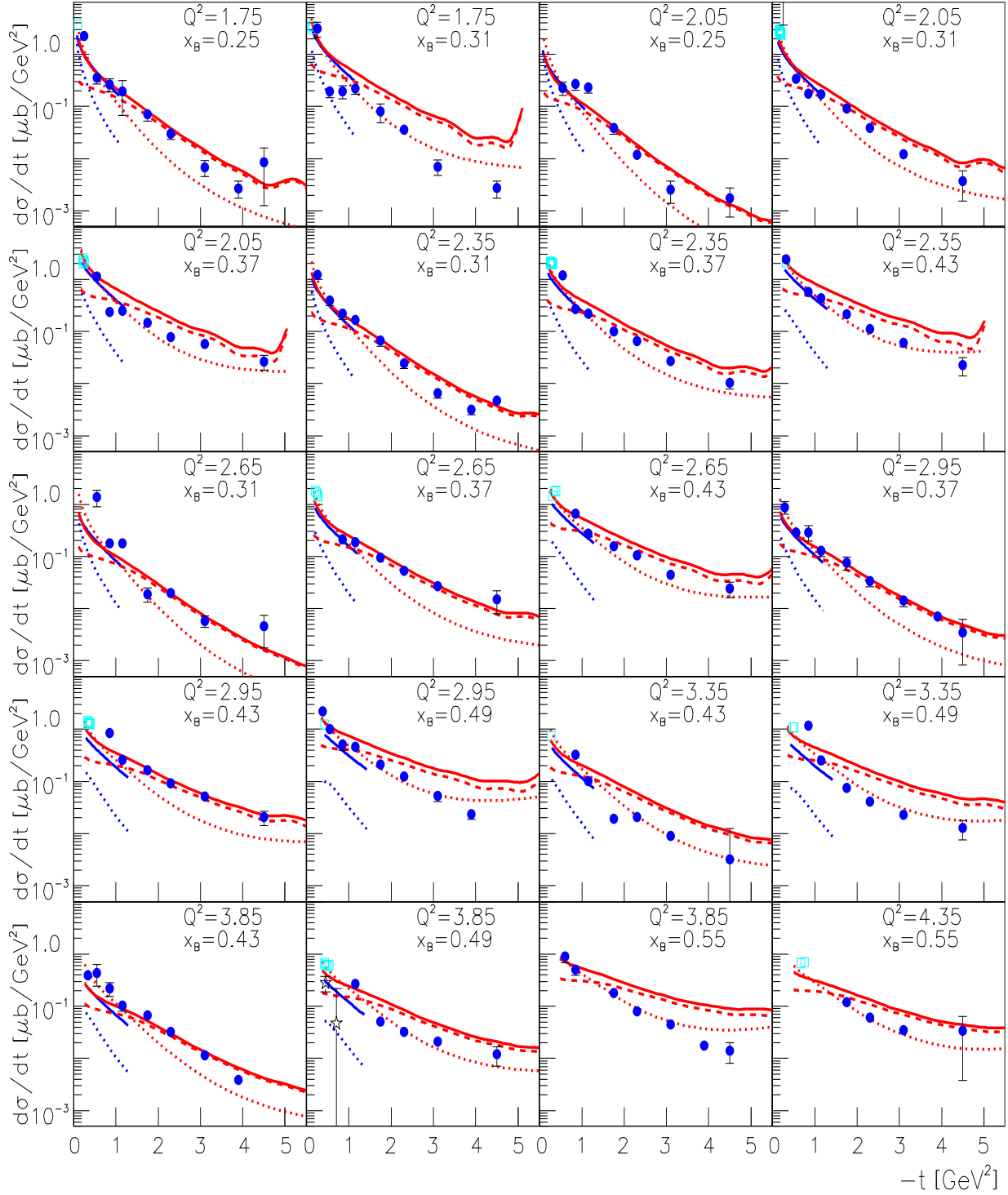


FIG. 13: (Color online) Differential cross section $d\sigma/dt$ [$\mu\text{b}/\text{GeV}^2$] integrated over ϕ_π^* at different (Q^2, x_B) bins. The dark filled blue circles show the results of this analysis. The light blue open squares ($d\sigma/dt$) [14], and black open stars ($d\sigma_L/dt$) [15] are the JLab Hall C data. The red solid ($d\sigma/dt$), dotted ($d\sigma_L/dt$), and dashed ($d\sigma_T/dt$) curves are the calculations from the Laget model [31] with (Q^2, t) -dependent form factors at the photon-meson vertices. The blue solid and dotted lines are the calculations of $d\sigma/dt$ and $d\sigma_L/dt$, respectively, of the GK model [17].

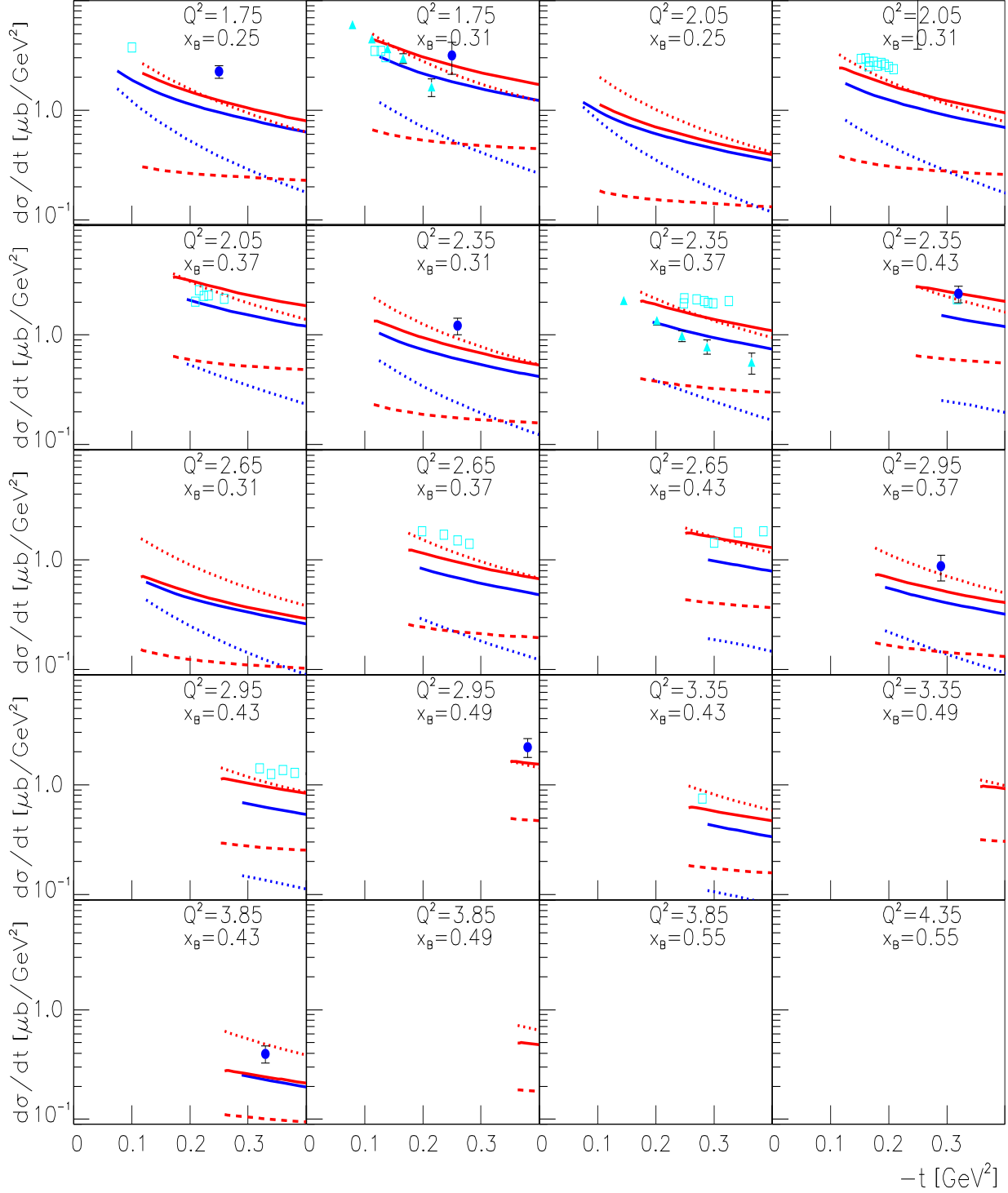


FIG. 14: (Color online) Differential cross section $d\sigma/dt$ [$\mu\text{b}/\text{GeV}^2$] versus t for $t < 0.4 \text{ GeV}^2$. The symbols are the same as in Fig. 13 with, in addition, the light blue filled triangles [13] which show the JLab Hall C separated $d\sigma_L/dt$ data.

We recall that in the GK model, the transverse part of the cross section is due to transversity GPDs. With such a contribution, the GK calculation describes then qualitatively our low- t data over our whole (x_B, Q^2) domain. This is remarkable, as one should note that the GK model was optimized for higher-energy kinematics (HERMES) and that no further adjustment of the parameters was done for the present CLAS kinematics. We should also note that the GK model is applicable only for small values of the ratio $-t/Q^2$. Outside this regime, additional higher-twist contributions that are not taken into account in the GK handbag formalism approach are expected. In Fig. 13, the GK calculation predicts that the transverse part of the cross section is dominating essentially everywhere in our kinematic domain. This means that, if the GK L/T ratio and its model-dependent way of treating handbag higher-twist corrections are correct, the exclusive π^+ electroproduction process provides an original and exciting way to access transversity GPDs. This obviously indicates the need of new L/T separated cross section data at large x_B , which will become available with the upcoming JLab 12-GeV upgrade.

B. $d\sigma/dt$ as a function of Q^2 at fixed t

Figure 15 shows the differential cross section $d\sigma/dt$ as a function of Q^2 at fixed x_B for various t values. As could be inferred from Fig. 13, where general agreement between the theoretical calculations and the experimental data was found, both the Laget and GK model calculations provide a roughly correct description of the magnitude and of the Q^2 dependence of $d\sigma/dt$. The Laget model seems to have a slightly steeper Q^2 dependence than the GK model. In any case, the limited precision and lever arm of our data doesn't allow favoring one model over the other. Because of the relatively low Q^2 range accessed in this experiment, higher-twist effects are expected and the leading-twist $1/Q^6$ dependence of σ_L is not expected. We fit our data with a $A/(Q^2)^n$ function and the exponents found, which have large error bars, indeed indicate in general a flatter Q^2 dependence than $1/Q^6$. This $1/Q^6$ asymptotic behavior must be reached at some point. The forthcoming JLab 12-GeV upgrade will allow to pursue the investigation of the onset of this $1/Q^6$ asymptotic behavior.

C. $d\sigma/dt$ as a function of W at fixed θ_π^*

Figure 16 shows our scaled cross sections $s^7 d\sigma/dt$ as a function of W for four Q^2 values and for four bins in $\cos\theta_\pi^*$: -0.01 ± 0.16 , 0.27 ± 0.1 , 0.42 ± 0.05 and 0.53 ± 0.06 . The lever arm in W is limited. At $\theta_\pi^* = 90^\circ$, where the scaling behavior is expected to set in most quickly, we

have only 2 or 3 data points in W depending on the Q^2 bin. It is therefore difficult to draw precise conclusions at this stage for the W -dependence at fixed Q^2 . Nevertheless, with these limited (but unique) data, one can say that, except maybe for the 3 data points at $Q^2=2.35$ GeV², the W -dependence of $s^7 d\sigma/dt$ does not appear to be constant. We also display in Fig. 16 the result of the Laget model. It gives, within a factor two, a general description of these large angle data. The W -dependence is very similar to the energy dependence that was observed in photoproduction [9]. In the same energy range as covered by the present study, real photon data exhibit strong deviations from scaling. Within the Laget model, these deviations are well accounted for by the coupling between the $n\pi^+$ and the ρN channels [33]. The JLab 12-GeV upgrade will allow to increase the coverage in W and check whether this finding remains valid in the virtual photon sector.

IX. SUMMARY

In summary, we have measured for the first time the cross sections of exclusive electroproduction of π^+ mesons off protons as a function of $-t = 0.1 - 5.3$ GeV², $x_B = 0.16 - 0.58$, and $Q^2 = 1.6 - 4.5$ GeV². We have compared our differential cross sections to two recent calculations based on hadronic degrees of freedom (Laget Regge) and on partonic degrees of freedom (GK handbag). Both models give a qualitative description of the overall strength and of the t -, Q^2 - and x_B - dependencies of the data. To achieve this, the Regge model needs the implementation of (Q^2, t) -dependent electromagnetic form factors while the handbag model needs the introduction of transversity GPDs. In detail, the two approaches differ in the relative contributions of the longitudinal and transverse parts of the cross section, in particular as x_B increases. Experimentally L-T separated cross sections, which can be foreseen to be extracted with the upcoming 12-GeV upgrade, are needed to distinguish between the two approaches. If the handbag approach finds confirmation, the $p(e, e'\pi^+)n$ process contains the outstanding potential to access transversity GPDs.

X. ACKNOWLEDGMENT

We acknowledge the outstanding efforts of the staff of the Accelerator and the Physics Divisions at Jefferson Lab that made this experiment possible. We also give many thanks to P. Kroll and S. Goloskokov for their calculation. The early work of D. Doré on this analysis is also acknowledged. This work was supported in part by the US Department of Energy, the National Science

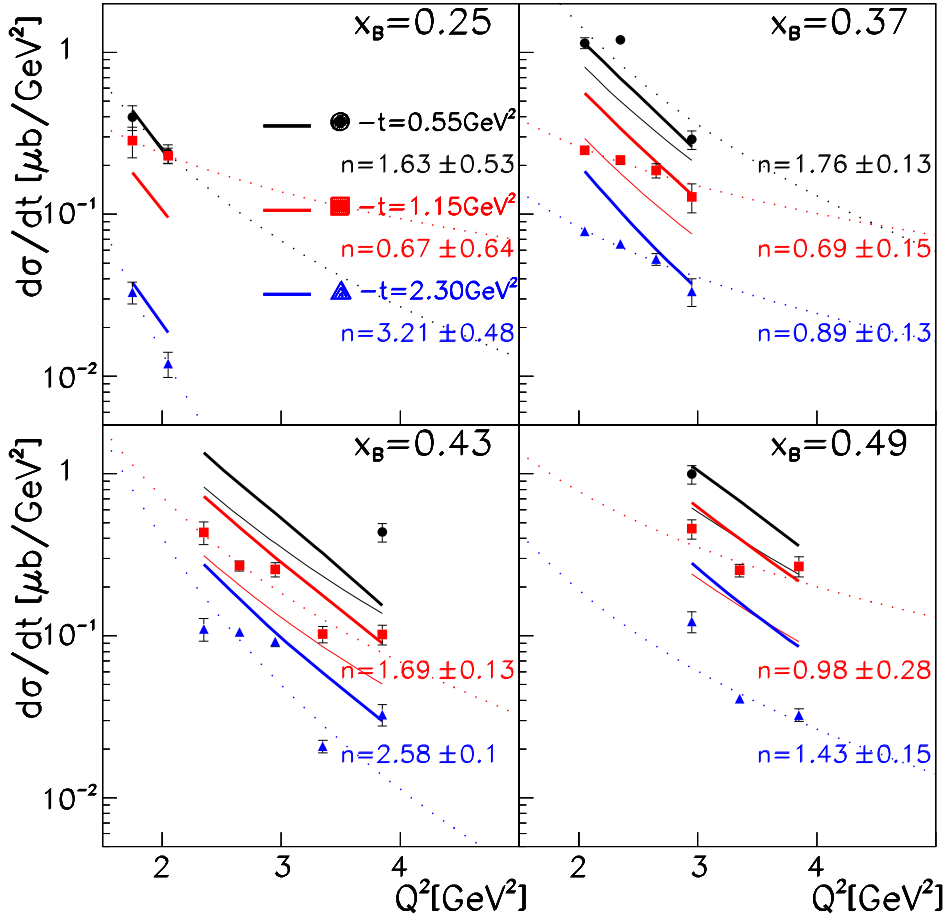


FIG. 15: (Color online) The differential cross section $d\sigma/dt$ [$\mu\text{b}/\text{GeV}^2$] versus Q^2 at fixed x_B for various t values. The dotted curves are the results of a fit by the function $A/(Q^2)^n$. The bold solid curves are the results of the Laget calculations [31] and the thin solid curves are the results of the GK calculations [17]. We recall that the GK calculation is only valid for $-t < \approx 1$ GeV^2 so that we do not display its result for $-t = 2.3$ GeV^2 . When only one solid curve is visible, it means that the Laget and GK calculations overlap.

97 Foundation, the Italian Istituto Nazionale di Fisica Nu- 5
 1 nucleare, the French Centre National de la Recherche Scien- 6
 2 tifique, the French Commissariat à l'Énergie Atomique, 7
 3 the United Kingdom's Science and Technology Facilities 8
 4 Council, and the National Research Foundation of Ko- 9

rea. The Southeastern Universities Research Association
 (SURA) operated the Thomas Jefferson National Accelerator Facility for the US Department of Energy under Contract No.DE-AC05-84ER40150.

-
- 9 [1] D. Müller, D. Robaschik, B. Geyer, F.-M. Dittes, and J. 17
 10 Horejsi, Fortschr. Phys. **42**, 101 (1994). 18
 11 [2] X. Ji, Phys. Rev. Lett. **78**, 610 (1997); Phys. Rev. D **55**, 19
 12 7114 (1997). 20
 13 [3] A.V. Radyushkin, Phys. Lett. B **380** (1996) 417; Phys. 21
 14 Rev. D **56**, 5524 (1997). 22
 15 [4] J. C. Collins, L. Frankfurt, and M. Strikman, Phys. Rev. 23
 16 D **56**, 2982 (1997). 24
- [5] S. V. Goloskokov, P. Kroll, Eur. Phys. J. C **65**, 137 (2010).
 [6] S. J. Brodsky and G. P. Lepage, Phys. Rev. D **22**, 2157 (1980).
 [7] S. J. Brodsky and G. R. Farrar, Phys. Rev. Lett. **31**, 1153 (1973); Phys. Rev. D **11**, 1309 (1975); V. Matveev *et al.*, Nuovo Cimento Lett. **7**, 719 (1973).
 [8] R. L. Anderson *et al.*, Phys. Rev. D **14**, 679 (1976); C.

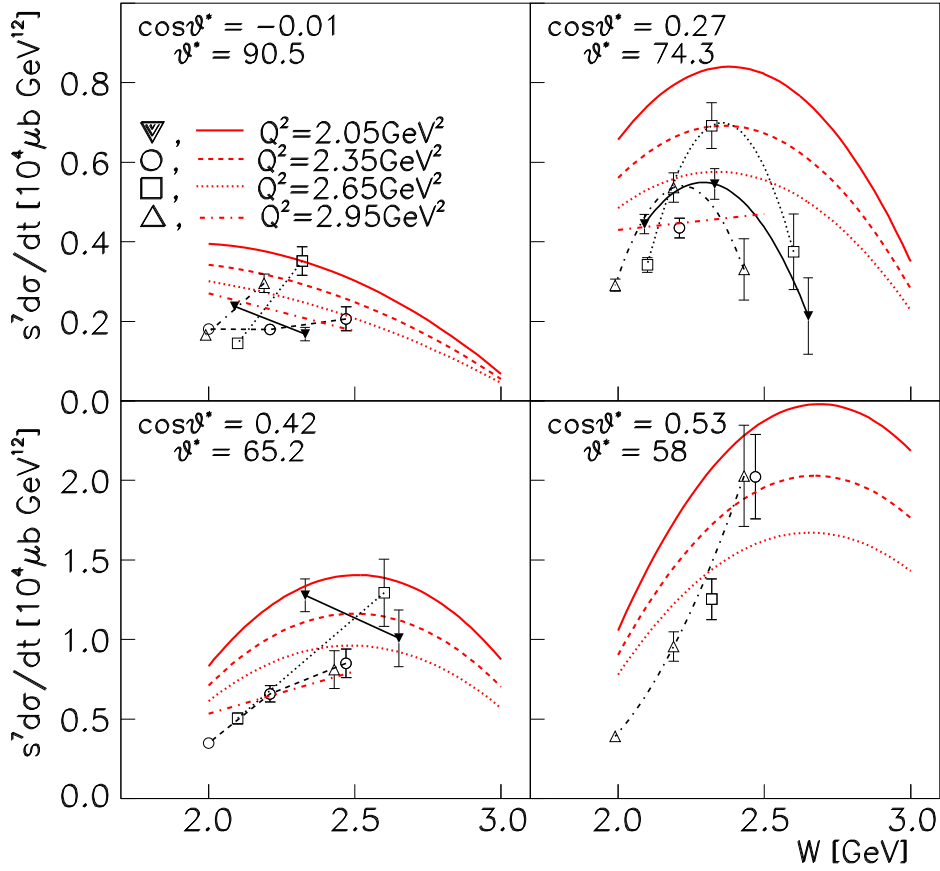


FIG. 16: (Color online) Scaled cross sections $s^7 d\sigma/dt$ [$10^4 \mu\text{b GeV}^{12}$] versus W from $\theta_\pi^* = 60^\circ$ to 90° for different Q^2 bins. Red curves from the Laget model [31]. The black curves show connection of data points which correspond Q^2 for the visibility purpose.

- 25 White *et al.*, Phys. Rev. D **49**, 58 (1994).
 1 [9] W. Chen *et al.*, Phys. Rev. Lett. **103**, 012301 (2009).
 2 [10] C. J. Bebek *et al.*, Phys. Rev. D **13**, 25 (1976).
 3 [11] C. J. Bebek *et al.*, Phys. Rev. D **13**, 1693 (1978).
 4 [12] A. Airapetian *et al.*, Phys. Lett. B **659**, 486 (2008).
 5 [13] H. P. Blok *et al.*, Phys. Rev. C **78**, 045202 (2008).
 6 [14] X. Qian *et al.*, Phys. Rev. C **81**, 055209 (2010).
 7 [15] T. Horn *et al.*, Phys. Rev. C **78**, 058201 (2008).
 8 [16] M. Vanderhaeghen, P. A. M. Guichon, and M. Guidal,
 9 Phys. Rev. D **60**, 094017 (1999).
 10 [17] S.V. Goloskokov, P. Kroll, Eur. Phys. J. A **47**, 112 (2011).
 11 [18] L. Mankiewicz, G. Piller and A. Radyushkin, Eur. Phys. J. C **10**, 307 (1999).
 12 [19] L. Frankfurt, P. Pobylitsa, M. Poliakov, M. Strikman,
 13 Phys. Rev. D **60**, 014010 (1999).
 14 [20] L.Y. Zhu *et al.*, Phys. Rev. Lett. **91**, 022003 (2003), Phys. Rev. C **71**, 044603 (2005).
 15 [21] J. Napolitano *et al.*, Phys. Rev. Lett. **61**, 2530 (1988); S. J. Freedman *et al.*, Phys. Rev. C **48**, 1864 (1993); J. E.
 16 Belz *et al.*, Phys. Rev. Lett. **74**, 646 (1995).
 17 [22] C. Bochna *et al.*, Phys. Rev. Lett. **81**, 4576 (1998).
 18 [23] E. C. Schulte *et al.*, Phys. Rev. Lett. **87**, 102302 (2001).
 19 [24] P. Rossi *et al.*, Phys. Rev. Lett. **94**, 012301 (2005); M. Mirazita *et al.*, Phys. Rev. C **70**, 014005 (2004).
 20 [25] B. Mecking *et al.*, Nucl. Instrum. Methods A **51**, 409 (1995).
 21 [26] K. Park *et al.*, Phys. Rev. C **77**, 015208 (2008).
 22 [27] E. Golovach, M. Ripani, M. Battaglieri, R. De Vita, private communication.
 23 [28] L. W. Mo, Y. S. Tsai, Rev. Mod. Phys. **41**, 205 (1969).
 24 [29] S. Stepanyan, private communication.
 25 [30] A. Afanasev *et al.*, Phys. Rev. D **66**, 074004 (2002).
 26 [31] J. M. Laget, Phys. Rev. D **70**, 054023 (2004).
 27 [32] M. Guidal, J. M. Laget and M. Vanderhaeghen, Nucl. Phys. A **627**, 645 (1997), Phys. Lett. B **400**, 6 (1997).
 28 [33] J. M. Laget Phys. Lett. B **685**, 146 (2010).